

See discussions, stats, and author profiles for this publication at: <https://www.researchgate.net/publication/262344639>

Elaboration and Rheological Investigation of Magnetic Sensitive Nanocomposite Biopolymer Networks

ARTICLE in MACROMOLECULES · APRIL 2014

Impact Factor: 5.8 · DOI: 10.1021/ma402655g

CITATIONS

3

READS

83

6 AUTHORS, INCLUDING:



[Cecilia Galindo-Gonzalez](#)

SOLEIL synchrotron

12 PUBLICATIONS 87 CITATIONS

[SEE PROFILE](#)



[Fayna Mammeri](#)

Paris Diderot University

27 PUBLICATIONS 494 CITATIONS

[SEE PROFILE](#)



[Souad Merah](#)

Paris Diderot University

129 PUBLICATIONS 1,742 CITATIONS

[SEE PROFILE](#)



[Alain Ponton](#)

Paris Diderot University

50 PUBLICATIONS 493 CITATIONS

[SEE PROFILE](#)

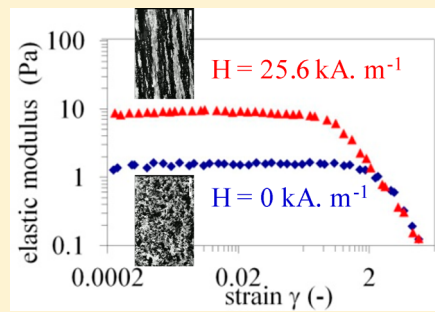
Elaboration and Rheological Investigation of Magnetic Sensitive Nanocomposite Biopolymer Networks

Cécilia Galindo-Gonzalez,[†] Stéphanie Gantz,[†] Laurence Oury,[‡] Fayna Mammeri,[‡] Souad Ammar-Merah,[‡] and Alain Ponton^{*,†}

[†]Matière et Systèmes Complexes (MSC), UMR 7057 CNRS & Université Paris Diderot-Paris 7, Case 7056, 75205 Paris, Cedex 13, France

[‡]Laboratoire Interfaces Traitements Organisation et Dynamique des Systèmes (ITODYS), UMR 7086 CNRS & Université Paris Diderot-Paris 7, Case 7090, 75205 Paris, Cedex 13, France

ABSTRACT: We propose the elaboration and study of rheological properties under continuous magnetic field of magnetic sensitive biopolymer-based nanocomposites. Magnetic iron oxide (maghemite) nanoparticles were synthesized by the polyol process and then functionalized by grafting organic bifunctional ligand for establishing electrostatic bonds between the sodium alginate chains of biopolymer and functionalized nanoparticles. The enhancement of rheological properties at low shear rate of these new magnetic soft nanocomposites was clearly demonstrated by the increase of yield stress and viscoelastic moduli in the linear viscoelastic domain with an increase of applied magnetic field, thus providing new functionality to these soft nanocomposites.



INTRODUCTION

During recent years, the development and applications of hydrogel nanocomposites,¹ more specifically as a new class of biomaterials, have attracted growing interest. Nanoparticles (NPs), e.g. gold, maghemite, silica, or nanomaterials such as carbon nanotubes (CNTs), can be dispersed in polymer solutions before being cross-linked or otherwise precipitated in a preformed polymer network. NPs can present on their surface reactive functional groups for specific interactions with the polymer chains, thus improving their final distribution. They can also be physically trapped inside the polymer in the form of cluster network.² In some cases, NPs can absorb specific electromagnetic stimuli and induce different effects which can be useful for local *in vivo* therapy. For instance, gold NPs may absorb selectively near-infrared light³ and, in certain conditions, cause photothermal effects. Maghemite NPs are able to generate heat when an alternating magnetic field is applied⁴ and potentially induce hyperthermia effects. The heat effect of magnetic nanoparticles is due to two main relaxation processes—the Brownian relaxation and the Neel relaxation—because of the small particle size. In that sense, the behavior of magnetorheological fluids composed of micro-sized particles dispersed in nonmagnetic media is different. In particular, the dispersion can be destabilized by sedimentation of micro-sized particles. Stability enhancement against gravity was reported for example either by adsorption of poly(acrylic acid) polymer on magnetite particles⁵ or by dispersion in an aqueous poly(ethylene oxide) solution⁶ as well as in polyurethane gel.⁷

Recent works on CNTs have shown that they can also be heated selectively by exposure to radio-frequency or near-infrared waves.⁸

Langer et al.⁹ evidenced such synergistic features in magnetic composites. They successfully incorporated ferromagnetic steel particles into a matrix of ethylene vinyl acetate copolymer, and by applying an oscillating static magnetic field at very low frequency, they modified the mechanical properties of the composite. They also evidenced that the variation in field of the particle–particle interactions and/or particle–magnet modulated the conformation of the polymer chains, which in turn changed the viscoelasticity of the polymeric matrix. They used these changes to control the release rate of bovine serum albumin, initially trapped between chains, offering real opportunities in the field of the controlled drug delivery. High-frequency magnetic field was also used to modulate pulsatile drug release from a ferrogel composed of gelatin cross-linked by genipin, reinforced by chitosan and magnetic nanoparticles.¹⁰ It was shown that cyclic exposures to high-frequency magnetic field induced controllable and repeatable release of vitamin B₁₂ used as a model drug.

Hilt et al.^{11–13} encapsulated model active molecules in magnetic hydrogels whose swelling properties are temperature-sensitive. They incorporated superparamagnetic Fe₃O₄ particles in negative temperature sensitive poly[N-isopropylacrylamide] (PNIPAm) and applied an alternating magnetic field in order to induce a local temperature increase. They observed a deflation of the gel and the release of the active molecule. Conversely, the temperature decreased in the absence of magnetic field, causing the swelling of the gel and slowing the drug release rate. They showed also that the modulation of the release of the

Received: December 30, 2013

Revised: March 3, 2014

Published: April 23, 2014

active molecule depended on the duration of application of the magnetic field as well as its molecular weight. Because of the decrease of the diffusion's efficiency of the active molecule when the gel is in a deflated state, the application of the magnetic field over longer times caused a decrease over time in the rate of release of the active molecule.

Temperature and magnetic field sensitivity was also used to separate temperature responsive poly(*N*-isopropylacrylamide) gel beads in a nonhomogeneous magnetic field.¹⁴

Clearly, whatever the type of the applied magnetic field, static or alternative, its stimulus on magnetic composites allows a controlled delivery of active agents and offers a smart *in vivo* therapeutic approach. Magnetic field is very few absorbed by tissues and does not exhibit clear side effects.

Focusing on drug delivery application, biocompatible drug vectors are mainly used. Among them, polymers such as PNIPAm, poly(ethylene oxide), or gelatin exhibit good biocompatibility and capabilities of release of active ingredients. Unfortunately, they are not degradable in biological conditions and may involve *in vivo* clearance problems requiring, in some cases, surgery to remove the implant after treatment. The choice of hydrogels as biocompatible and biodegradable polymers should overcome such a drawback. Hawkins et al.¹⁵ embedded, for instance, magnetic NPs in degradable poly(β -amino ester) hydrogels which present a hydrolytic degradation dependent on the temperature. These authors have shown that the application of alternating magnetic field allows temperature increase and induces, in more rapid degradation rate, the release of green tea polyphenols, chosen as a model drug.

Nevertheless, exploring the use of dc magnetic fields and low frequency on such magnetic hydrogels, some authors showed that the application of such fields can induce attractions between particles and can modify the pore size leading to the modulation of the diffusion of the drug effectiveness.^{16,17} To prevent such phenomenon, it is important to improve the distribution of magnetic NPs, usually iron oxide NPs, into the polymeric matrix and their attachment to the organic chains, e.g., through their functionalization by bifunctional small molecules, also called coupling agents, bearing a group able to be grafted to the particle's oxide surface as well as another one able to interact more or less strongly with the polymers.

In this context, we investigated the magnetorheological properties of a magnetic sensitive nanocomposite biopolymer-based materials made from positively charged maghemite NPs incorporated in negatively charged polymer chains. For this purpose, we selected sodium alginate polymer, a natural polysaccharide composed of linear copolymer containing β -1,4-D-mannuronate (M) and α -1,4-L-guluronate (G) units in various proportions and sequences depending on the season, age, and the part of the plant used for extraction. Bearing one carboxylate group in each M or G unit, sodium alginate is a highly negatively charged polyelectrolyte at neutral or basic pH. Besides, the iron oxide NPs were functionalized by 3-aminopropyltriethoxysilane, bearing a terminal amine function. In aqueous solution, the positively charged functional group (NH_3^+) is available for electrostatic bindings with negatively charged carboxylate groups COO^- of sodium alginate chains. The influence of this coupling agent on the rheological properties under controlled magnetic field was investigated for a better understanding of such magnetic complex nanocomposite materials, before evaluating them as drug vectors and measuring the kinetic of their drug release mechanism.

MATERIALS AND METHODS

Synthesis. **Magnetic NPs.** Maghemite ($\gamma\text{-Fe}_2\text{O}_3$) NPs were synthesized by forced hydrolysis of metallic salts, namely iron acetates, in a polyol solvent.^{18,19} Typically, 4.3 g of $\text{Fe}(\text{CH}_3\text{CO}_2)_2$ (ACROS, 95%) was dissolved in 250 mL of diethylene glycol (DEG) under mechanical stirring before heating up to boiling at $6\text{ }^\circ\text{C min}^{-1}$. A given volume of distilled water (1 mL) was also added to get a hydrolysis ratio, defined as the molar ratio between water and iron cations, of $h = 2$. The mixture was maintained under reflux for 3 h before cooling down to room temperature (RT). In these operating conditions, iron oxide particle of a size ranging between 10 and 12 nm should be obtained. A black magnetic powder, assumed to be magnetite (Fe_3O_4), was then isolated by addition of acetone (polyol/acetone = 1/1 v/v) and centrifugation at 22 000 rpm for 20 min. The recovered powder was then washed with boiling water several times, to reduce magnetite into maghemite. A dark brown and magnetic powder was then recovered by centrifugation and finally dried in air at $50\text{ }^\circ\text{C}$.

Hybrid NPs. Maghemite nanoparticles were then functionalized (Figure 1) by grafting 3-aminopropyltriethoxysilane, quoted here-

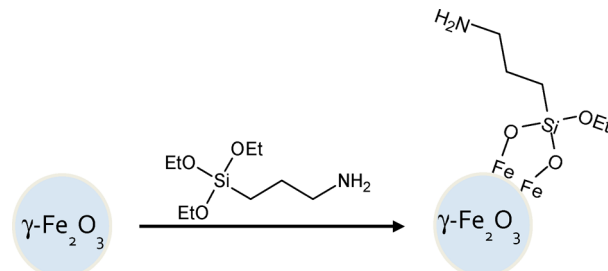


Figure 1. Schematic representation of the maghemite NPs functionalized by APTES.

after APTES (Aldrich, 99%). The experimental protocol is based on the study of Caruntu et al.²⁰ As-produced NPs were dispersed by sonication for a few minutes in 4 mL of methanol. Afterward, 100 mL of ethanol was added under sonication. Then, 400 μL of APTES was mixed to the solution by mechanical stirring for 1 h and heated up to boiling for 2 h under an argon atmosphere. Functionalized NPs were then collected with a magnet, washed with ethanol, and dried.

Nanocomposites. The sodium alginate was extracted from marine brown algae and used as a white dried powder (Sigma-Aldrich). It was dissolved as-purchased, in deionized water (50 g L^{-1}), to obtain an anionic polyelectrolyte in which the carboxylate anion charges are counterbalanced by those of sodium cations. The dissolution was carried out at RT under mechanical stirring (300 rpm) for 14 h. At the same time, solid APTES-grafted NPs were dissolved in deionized water by mixing a few minutes with a vortex and then by ultrasonication at RT in order to minimize the particle clustering. Afterward, deionized water was added to a known volume of the stock solution of sodium alginate. After a mechanical stirring of 5 min, a volume of aqueous solution of magnetic nanoparticles was finally introduced to obtain the two studied samples with a constant sodium alginate concentration ($C_{\text{alg}} = 18\text{ g L}^{-1}$) and two volume fractions of nanoparticles ($\Phi_{\text{NP-APTES}} = 0.5\%$ and $\Phi_{\text{NP-APTES}} = 1\%$).

Characterization. **Structural and Microstructural Analyses.** The structure of bare and functionalized maghemite NPs was analyzed using X-ray diffraction (XRD) with a Panalytical diffractometer equipped with a X'celerator detector and a cobalt X-ray tube ($\lambda = 1.7889\text{ \AA}$) in a θ - θ Bragg-Brentano reflection configuration in the 10° - 100° angular range (with a step of 0.025 for 2 s). Their microstructure was checked by transmission electron microscopy (TEM) using a JEOL-100-CX II microscope operating at 100 kV. APTES grafting was monitored through FTIR spectroscopy using the KBr technique on a Bruker Equinox spectrometer working in the 4000 - 500 cm^{-1} energy range with a resolution of 4 cm^{-1} . Besides, the chemical composition was checked using an energy dispersive spectrometer (EDX) mounted on a JEOL-JSM 6100 scanning electron

microscope (SEM) working between 20 and 25 kV. X-ray photoelectron spectroscopy (XPS) measurements were performed on as-prepared and functionalized NPs using a Thermo VG ESCALAB 250 instrument equipped with a microfocused, monochromatic Al $K\alpha$ X-ray source (1486.6 eV) and a magnetic lens. The X-ray spot size was 500 μm (15 kV, 150 W). The spectra were acquired in the constant analyzer energy mode with pass energy of 150 and 40 eV for the general survey and the narrow scans, respectively. The samples were fixed on sample holders and outgassed in the fast entry airlock (2×10^{-7} mbar). The "Avantage" software was used for data acquisition and processing. The C 1s line of 285 eV was used as a reference (adventitious carbon) to correct the binding energies for charge correction.

Magnetic Measurements. The magnetic properties of maghemite NPs and their related hybrids were inferred from field-dependent magnetization curves measured on a Quantum Design MPMS-SS SQUID magnetometer at 300 K. The external magnetic field was varied in the -4000 and $+4000$ kA m^{-1} range. Temperature-dependent magnetization plots were also measured at low field (15.9 kA m^{-1}) in the temperature range varying from 5 to 330 K in the field cooled (FC) and zero-field cooled (ZFC) modes. The particles were slightly compacted in a diamagnetic plastic sampling tube to avoid their displacement during measurements.

Rheological and Magnetorheological Measurements. The rheological measurements were performed with a rheometer Mars II (Thermo Fisher Scientific) fitted with a magnetic cell developed in the MSC laboratory in order to apply continuous magnetic field to the sample during the measurements. This device consisted of a mechanical part and a magnetic part. The former was a cone and plate geometry (60 mm in diameter and an angle of 1°) made of nonmagnetic material. The latter was composed of two coils, which were placed on both sides of the cone-plate geometry mounted on the rheometer with the bottom plate placed in the upper part of the lower coil. This configuration allowed creating a homogeneous magnetic field perpendicular to the shear. An electric current of variable intensity between 0 and 25 A induced between the coils separated by a 20 mm spacer a magnetic field strength between 0 and 31.9 kA m^{-1} . The homogeneity of the magnetic field was tested by measuring the field at 25.0 ± 0.2 $^\circ\text{C}$ for four current intensity values with a gaussmeter along two orthogonal diameters of the plate at the center and in six points. The measured field was found constant between $\pm 2\%$ inside the central area (40 mm diameter) and $\pm 6\%$ at the border of the plane (60 mm diameter). The temperature of the sample was controlled by a Peltier device linked to a PID device during rheological measurements and kept constant to 25.0 ± 0.3 $^\circ\text{C}$. For oscillatory measurements, a ramp of sinusoidal strain with constant frequency $f = 1$ Hz and variable amplitude between 10^{-4} and 1000 was first applied. Frequency dependence of the elastic G' and loss G'' moduli was then measured between 0.01 and 100 Hz at constant strain amplitude in the linear viscoelastic domain. Steady-state flow curves were obtained by increasing the shear rate from 0.01 and 2000 s^{-1} . The duration of each step was varied from 60 to 600 s depending of the value of imposed shear rate in order to measure stationary value of shear stress. When a magnetic field was applied, the following procedure was used: after insertion of the sample on the plate of magnetic cell, the magnetic field was switched on for 500 s. This waiting time was long enough to ensure an equilibrium state of the buildup of field-induced structures in biopolymer network and thermal steady state.

Optical Microscopic Observations. Optical microscopy observation was carried out using a laboratory made special device (Figure 2) allowing the application of a magnetic field during the observations. Two moving permanent magnets were placed in slots of a nonmagnetic circular plate. The positions of the two magnets were fixed by screws creating a magnetic field from 3.2 to 23.9 kA m^{-1} in the same range as for rheological measurements. A rectangular capillary filled with sodium alginate solutions incorporating APTES-grafted NPs was placed at the middle of the plate perpendicularly to the direction of the magnetic field. The capillary was closed on both ends by modeling clay to avoid evaporation. The observation was performed by a Nikon microscope with a resolution objective of 10 \times

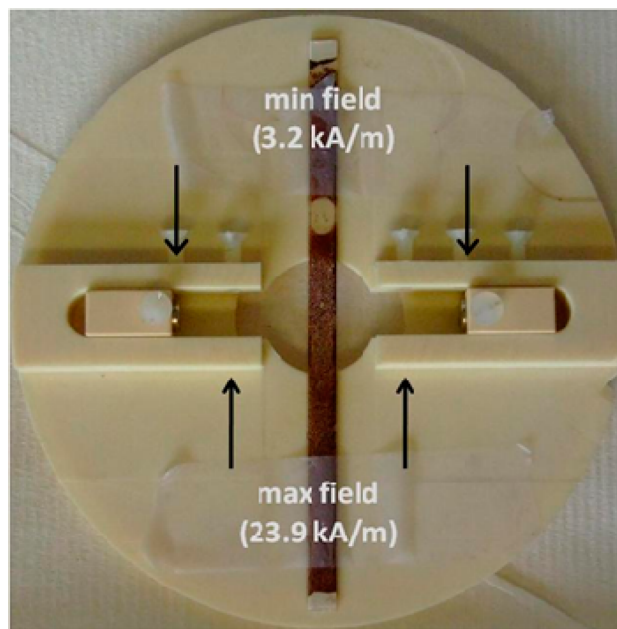


Figure 2. Home-made device for optical observation under application of a magnetic field.

at two values of magnetic field strengths (3.2 and 23.9 kA m^{-1}). The magnetic field was applied for 5 min before recording images analyzed by freeware software.

RESULTS AND DISCUSSION

Properties of the Positively Charged Maghemite NPs.

The XRD patterns of the as-produced brown iron oxide particles and their related hybrids are very close to each other. They show broadened diffraction peaks (Figure 3) that can unambiguously be attributed to iron oxide and indexed as an iron oxide phase with cubic spinel structure.

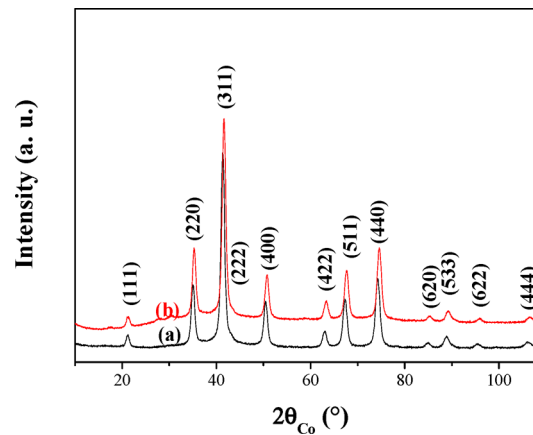


Figure 3. XRD patterns of the as-produced maghemite particles (a) and their related nanohybrids resulting from the functionalization by APTES (b).

The refined cell parameter using the MAUD program, assuming a pseudo-Voigt diffraction peak profile,²¹ was found to be equal to $8.370(5)$ \AA , very close to that of bulk maghemite.²² Rietveld refinements also allowed the estimation of the mean coherent diffraction domain size. It is found to be about 11 nm. Pictures recorded on bare and hybrid NPs were found to be quite similar. Both samples appeared to be

constituted by roughly spherical, highly crystallized, and almost uniform in size single crystals. The particle size was obtained from the recorded TEM images (Figure 4) using a digital

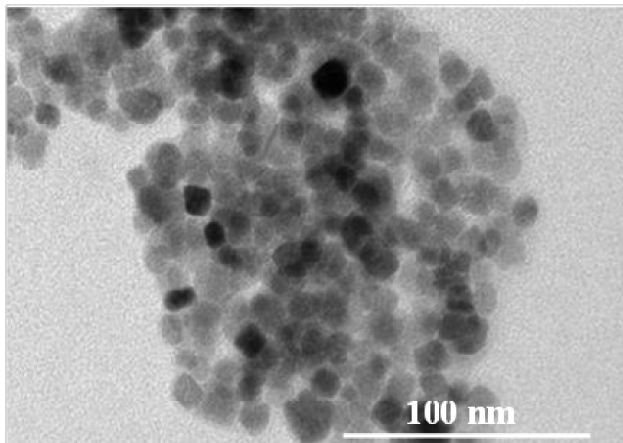


Figure 4. TEM image of an assembly of as-produced maghemite NPs.

camera and SAISAM software (Microvision Instruments), calculating the surface-average particle diameter through a statistical analysis performed by counting about 300 particles considered to be spherical. The mean diameter was found to about 11 ± 2 nm, very close to the mean diffraction domain size. Nevertheless, the particles functionalized by APTES seemed to be less agglomerated (not shown), suggesting an effective APTES grafting.

The FTIR spectra of the as-produced brown particles and their related hybrids were compared to that of fresh APTES (Figure 5). Both spectra exhibit a strong multiple band at 700,

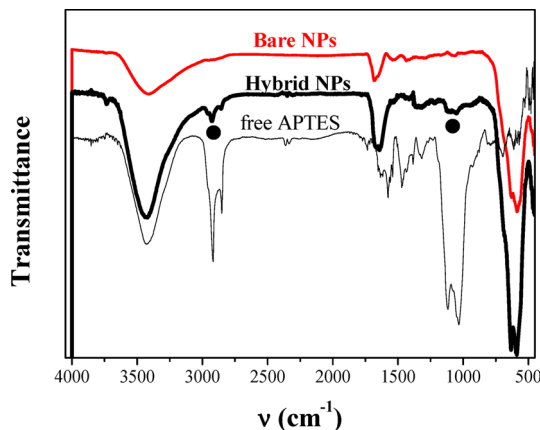


Figure 5. FTIR spectra of bare and APTES-grafted maghemite NPs compared to that of free APTES. The main bands related to the silane species are marked by a dot on the spectrum.

650, and 590 cm^{-1} due to the stretching vibration of the Fe–O particle skeleton in maghemite (when only the peak at 590 cm^{-1} is expected for magnetite).²² Additional vibration bands appeared after the reaction with APTES, particularly at around 2925 and 1100 cm^{-1} assigned to the stretching symmetric vibration of C–H (in CH_2) and Si–O bonds of APTES, respectively.²³

To remove any ambiguity on the issue of APTES grafting, EDS analysis was carried out on both samples. It clearly evidenced the iron oxide nature of the particles by the

fluorescence peaks of iron and oxygen atoms and confirmed APTES grafting by the appearance of the fluorescence peak corresponding to silicon (Figure 6). A Kaiser assay performed

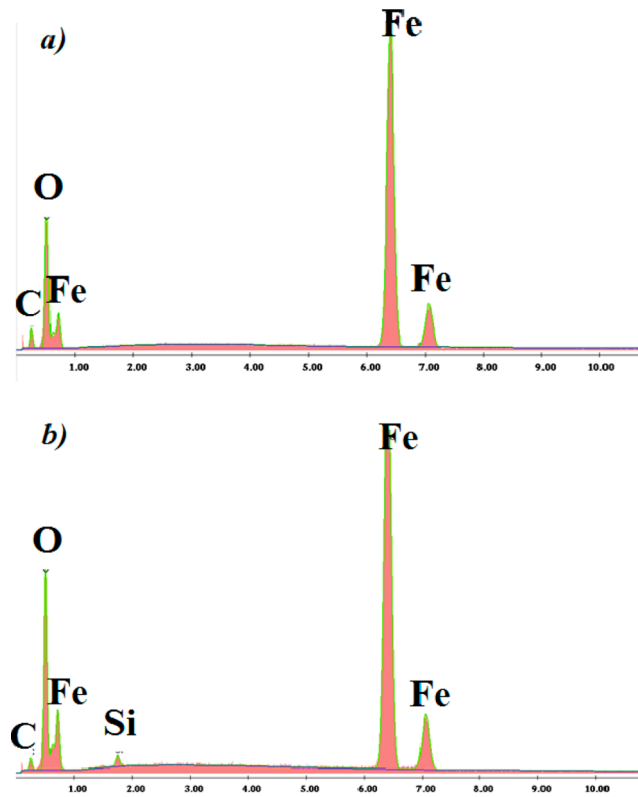


Figure 6. EDS analysis of bare (a) and APTES-grafted (b) NPs.

on NPs shows the presence of about 300 amine moieties per nanoparticle, which implies an APTES coating close to the monolayer and corresponds qualitatively to a grafting density of $1.05\text{ molecule nm}^{-2}$.

Then, XPS survey spectra of both bare and hybrid NPs were recorded and are presented in Figure 7. The survey spectrum of bare NPs exhibits the characteristic peaks corresponding to iron oxide: Fe 2p (711 eV), O 1s (530 eV) with a satisfying atomic ratio of $\text{Fe}/\text{O} = 2/3$. The C 1s peak could be fitted with three

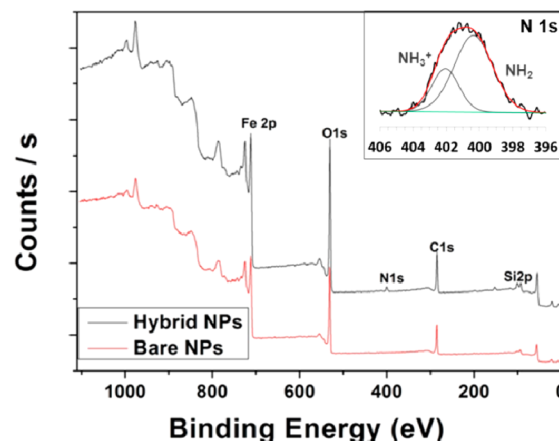


Figure 7. XPS survey spectra of bare and hybrid nanoparticles. Inset: high-resolution spectrum of N 1s.

components, centered at 285.0 eV, 286.5, and 288.7 eV, corresponding to adventitious aliphatic carbon and C—O/C=O bonds of residual polyol molecules.

The survey spectrum of hybrids NPs exhibits two new peaks characteristic of Si 2p at 101.3 eV and N 1s. The latter (see inset in Figure 7) exhibits two components: one centered on 402.5 eV, corresponding to protonated amine groups (NH_3^+), and the second, centered on 400.6 eV, corresponding to free amine groups (NH_2).

Besides, the magnetic properties of bare and hybrid NPs were determined using conventional magnetometry. The thermal variation of the magnetic susceptibility χ was recorded for both samples in the FC and ZFC modes at a magnetic field of 15.9 kA m⁻¹ (Figure 8). It systematically evidenced a net

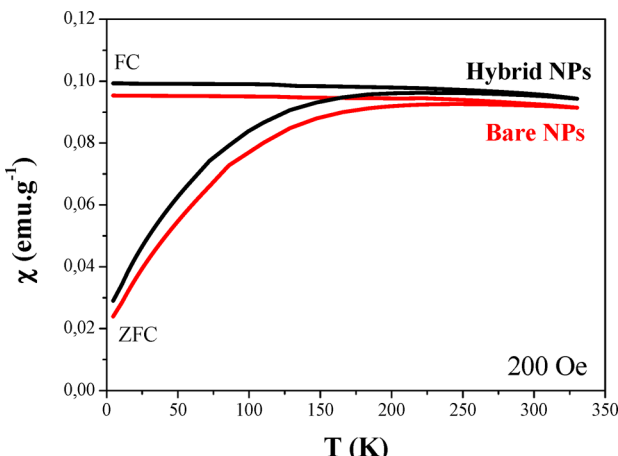


Figure 8. Thermal variation of the magnetic susceptibility of bare and APTES-grafted NPs recorded in the FC and ZFC modes under a magnetic field of 15.9 kA m⁻¹.

irreversibility between the FC and ZFC segments, in agreement with a superparamagnetic behavior. The blocking temperature (T_B) value, which is characteristic of the transition from the blocked ferromagnetic state of these NPs to their thermal fluctuating one, is given by the temperature position of the maximum of the ZFC- $\chi(T)$ curve, in agreement with the usual procedure. It was found to be around 275 K for as-prepared NPs and of 245 K for functionalized NPs. This discrepancy is mainly due to particle-particle distance change when APTES was grafted. Indeed, it is assumed that increasing interparticle spacing, the maxima of the mean blocking temperatures shifts toward lower temperatures and inversely, decreasing interparticle spacing provides a T_B value increase.^{24–27}

Superparamagnetic behavior was also confirmed by the magnetization (M) variation as a function of the magnetic field at $T > T_B$. Neither remanence nor coercivity was observed in the $M(H)$ loops with a magnetization which tends to saturation at field as high as 4000 kA m⁻¹, namely 5 T (Figure 9). The plots appeared to be almost similar for both samples. Only a very slight increase of the magnetization at high field was observed for hybrid NPs, 69.9 versus 69.7 kA m⁻¹ kg⁻¹ for bare ones (see the inset in Figure 9), in agreement with dipolar interaction strength decreases. Indeed, usually, the interparticle interactions, mainly dipolar ones, induce a collective behavior between superparamagnetic particles, decreasing their total magnetization. This decrease remained quite negligible in the present case since it is counterbalanced by the magnetization

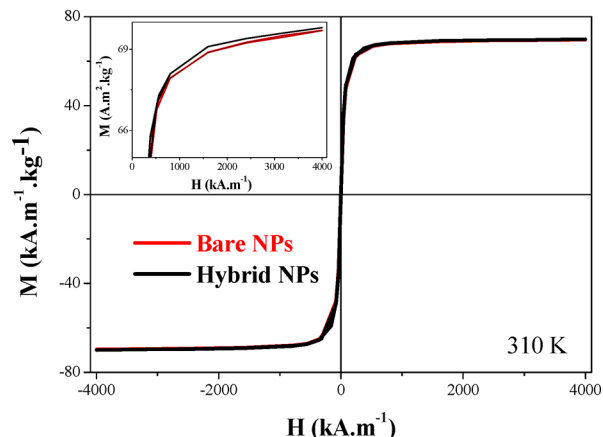


Figure 9. Variation of the magnetization versus magnetic field at 310 K. A zoom of the high field $M(H)$ segment is given for both samples in the inset.

decrease of the hybrids due to the diamagnetic contribution of the organic grafted layer.

As a conclusion, the magnetic properties of APTES-grafted NPs were found to be very close to those of bare maghemite NPs, encouraging their use as magnetic-field-sensitive agent for biopolymer structuration. This is discussed in the following section.

Oscillatory Measurements. Viscoelastic properties of the produced magnetic nanocomposites were first investigated by oscillation measurements. Without magnetic field (0 kA m⁻¹), the strain dependence of elastic G' and loss moduli G'' is the one classically observed for a polymer solution at a concentration higher than the entanglement concentration ($C_e \sim 2.5 \text{ g L}^{-1}$ for aqueous solutions of sodium alginate in this study). Both G' and G'' are constant in the linear viscoelastic domain until a critical strain above which a decrease of moduli is observed (Figures 10a,b) corresponding to the disentanglement of the polymer chains and shear thinning behavior as observed on flow measurements (see Characterization section). A most first interesting feature is the increase of moduli in the linear viscoelastic domain when the magnetic field strength is increased with a more pronounced effect for G' (Figure 10a) than for G'' (Figure 10b).

As shown in Figure 11 where the mean values in the linear viscoelastic domain of elastic ($G'\text{LVD}$) and loss ($G''\text{LVD}$) moduli at 1 Hz are plotted as a function of magnetic field strength, a fluid ($G''\text{LVD} > G'\text{LVD}$) to solid ($G''\text{LVD} < G'\text{LVD}$) viscoelastic transition is clearly observed for the highest volume fraction of nanoparticles ($\Phi_{\text{NP-APTES}} = 1\%$) in the studied range of magnetic field. A second main result is the decrease of critical strain as the magnetic field strength is increased (Figure 12).

The frequency dependence of elastic modulus at constant strain (0.01) in the linear viscoelastic domain at different magnetic field strengths for aqueous solution of sodium alginate ($C_{\text{alg}} = 18 \text{ g L}^{-1}$) with magnetic NPs ($\Phi_{\text{NP-APTES}} = 1\%$) confirms the enhancement of elastic properties observed in the strain dependence of the elastic and loss moduli in the linear viscoelastic domain (Figures 10) by increasing magnetic field strength until around a frequency of 3 Hz above which all the curves superpose (Figure 13a).

The same behavior is also observed for loss moduli (Figure 13b), and a critical frequency defined by the crossover of loss

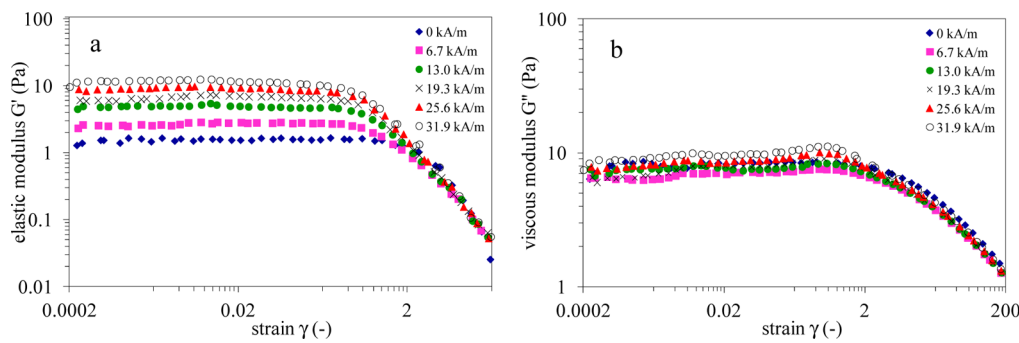


Figure 10. Variation of elastic (a) and loss (b) moduli as a function of strain and constant frequency of 1 Hz at different magnetic field strengths for aqueous solution of sodium alginate ($C_{\text{alg}} = 18 \text{ g L}^{-1}$) with magnetic nanoparticles ($\Phi_{\text{NP-APTES}} = 1\%$).

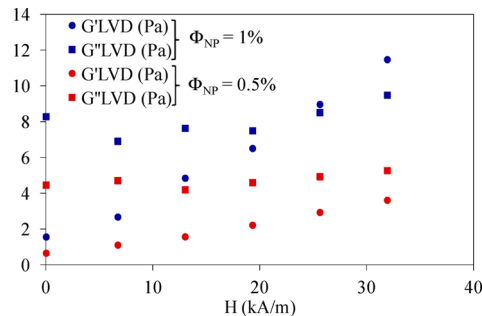


Figure 11. Variation of mean values in the linear viscoelastic domain of elastic (G' LVD) and loss (G'' LVD) moduli at 1 Hz as a function of magnetic field strength for aqueous solution of sodium alginate ($C_{\text{alg}} = 18 \text{ g L}^{-1}$) with magnetic nanoparticles ($\Phi_{\text{NP-APTES}} = 0.5\%$ and $\Phi_{\text{NP-APTES}} = 1\%$).

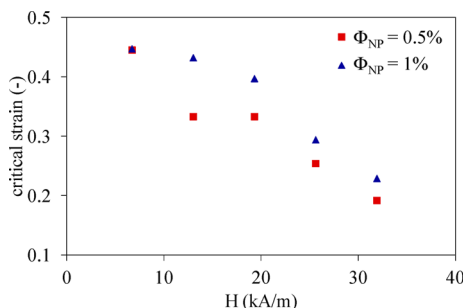


Figure 12. Variation of critical strain (strain at the end of linear viscoelastic domain) as a function magnetic field strength for aqueous solution of sodium alginate ($C_{\text{alg}} = 18 \text{ g L}^{-1}$) with magnetic nanoparticles ($\Phi_{\text{NP-APTES}} = 0.5\%$ and $\Phi_{\text{NP-APTES}} = 1\%$).

and elastic moduli can be defined for each magnetic field strength (Figure 14).

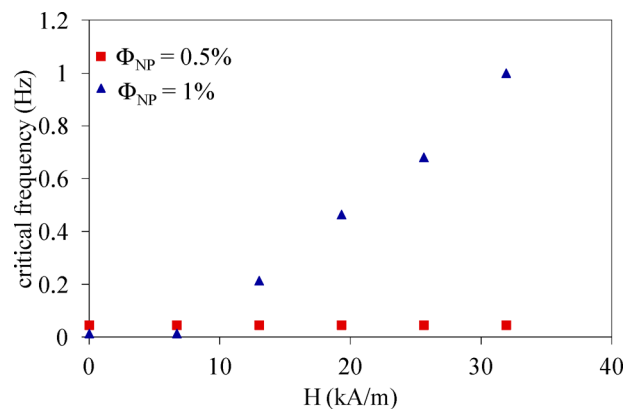


Figure 14. Variation of critical frequency (frequency for the crossover of G' and G'') as a function magnetic field strength for aqueous solution of sodium alginate ($C_{\text{alg}} = 18 \text{ g L}^{-1}$) with magnetic nanoparticles ($\Phi_{\text{NP-APTES}} = 0.5\%$ and $\Phi_{\text{NP-APTES}} = 1\%$).

To understand the increase of the viscoelastic moduli observed both by strain (Figures 10) and frequency (Figures 13) sweeps by increasing the magnetic field strength, a schematic representation of the complex structure of nanocomposite biopolymer-based material could be proposed (Figure 15a). The streamlines of the magnetic field are deformed near the NPs where magnetic north and south poles were created. Because of the attraction between two opposite dipoles, the distance between NPs in the direction of the magnetic field decreases by increasing the magnetic field

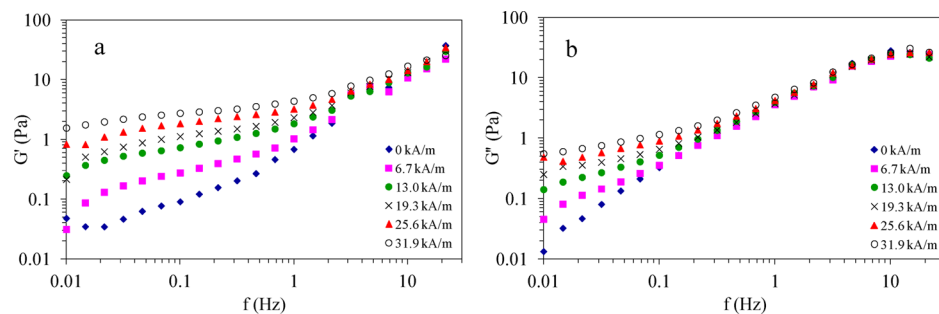


Figure 13. Variation of elastic (a) and loss (b) moduli as a function of frequency and constant strain of 0.01 at different magnetic field strengths for aqueous solution of sodium alginate ($C_{\text{alg}} = 18 \text{ g L}^{-1}$) with magnetic nanoparticles ($\Phi_{\text{NP-APTES}} = 1\%$). It should be noted that all points are superposed above a frequency of about 3 Hz.

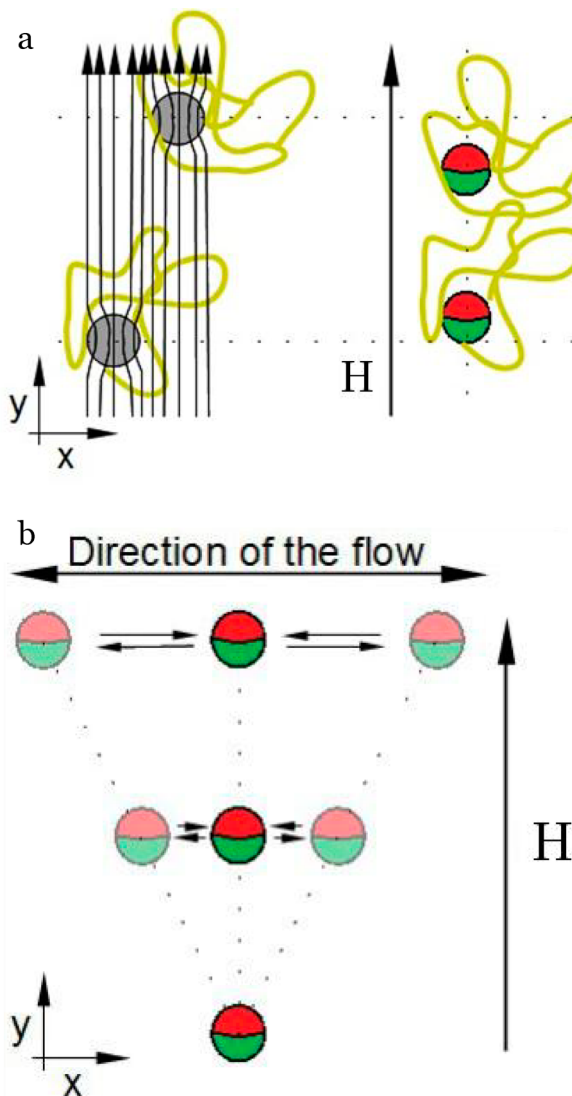


Figure 15. Schematic representation of complex structure of biopolymer chains with attached NPs (or clustered NPs) under application of a magnetic field at small strain (a) and high strain (b). In this case (b), the sodium alginate chains are not represented to simplify the figure.

strength. APTES-grafted NPs being attached to the sodium alginate chains, these later become closer to each other. This could explain the higher increase of elastic modulus than the loss modulus and the decrease of the critical strain. Indeed shear stress is higher ($\sigma = G' \Delta x / \Delta y$) when the distance of two NPs is lower (e.g., when increasing magnetic field strength) and polymer chains are disentangled at lower strain.

In the nonlinear viscoelastic domain, the displacement in the shear direction (x -direction in Figure 15b) should be considered. The NPs are accelerated in x -direction with a higher inertia. Furthermore, the distance in the x -direction between NPs increases with the increasing strain. Because of the low magnetic forces and noninteraction between NPs, the shear forces are higher than the magnetic forces inducing a decrease of moduli.

Flow Measurements. From the steady-state flow measurements, the different curves of the viscosity as a function of shear rate at different values of magnetic field strength exhibit an increase of the viscosity at low shear rate when the magnetic

field strength is increased (Figure 16). When the shear rate is increased, the curves for the different values of the magnetic field superimposed.

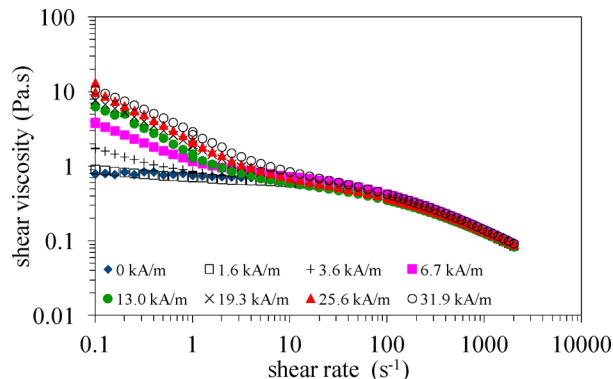


Figure 16. Variation of shear viscosity as a function of shear rate at different values of the external magnetic field strengths for aqueous solution of sodium alginate ($C_{\text{alg}} = 18 \text{ g L}^{-1}$) with magnetic NPs ($\Phi_{\text{NP-APTES}} = 1\%$).

The increase in the viscosity at low shear rate is the signature of a yield stress which was obtained by fitting the flow curves for shear rate between 0.01 and 10 s⁻¹ with the Herschel–Buckley model:

$$\sigma = \sigma_s + K \dot{\gamma}^n \quad (1)$$

where σ_s is the yield stress, K the consistency index, and n the shear thinning exponent.

The yield stress (Figure 17a) and the consistency index (Figure 17b) increase with a saturation trend when the magnetic field strength is increased due to a structuration of the nanocomposite material, in agreement with the oscillatory measurements. This nonmonotonic magnetic field dependence of yield stress was also reported in magnetorheological fluids. In a first low field domain the interparticle forces and shear stresses are predicted to vary quadratically with applied field. In a second intermediate field domain the yield stress is predicted to vary with $H^{3/2}$ due to a saturated magnetization of the particles in chains aligned along the field direction.²⁸ However, these predictions are difficult to apply to the results of this study due to the difference of microsized particles in magnetorheological fluids and magnetic nanoparticles as outlined in the Introduction and also to the absence of interaction effects between polymer chains and magnetic particles into models of the rheology of suspensions of nonlinearly magnetizable particles.

Conversely, the shear thinning exponent (Figure 18) decreases from a value of 0.93 very close to 1, corresponding to a plastic behavior up to 0.65. This behavior is observed in other kinds of magnetic fluids, such as ferrofluids²⁹ or inverse ferrofluids,³⁰ and these experimental values of n are very close to the theoretical values predicted for deformation of cylindrical aggregates and for chainlike aggregates ($n = 2/3$) which rotate before breaking.³¹

As for oscillatory measurements, the magnetic field induced structuration could be explained by a decrease of distance between magnetic nanoparticles linked to the sodium alginate chains at small shear rate.

Microscopic Observation. As previously mentioned, all the results obtained in the rheological measurements show that

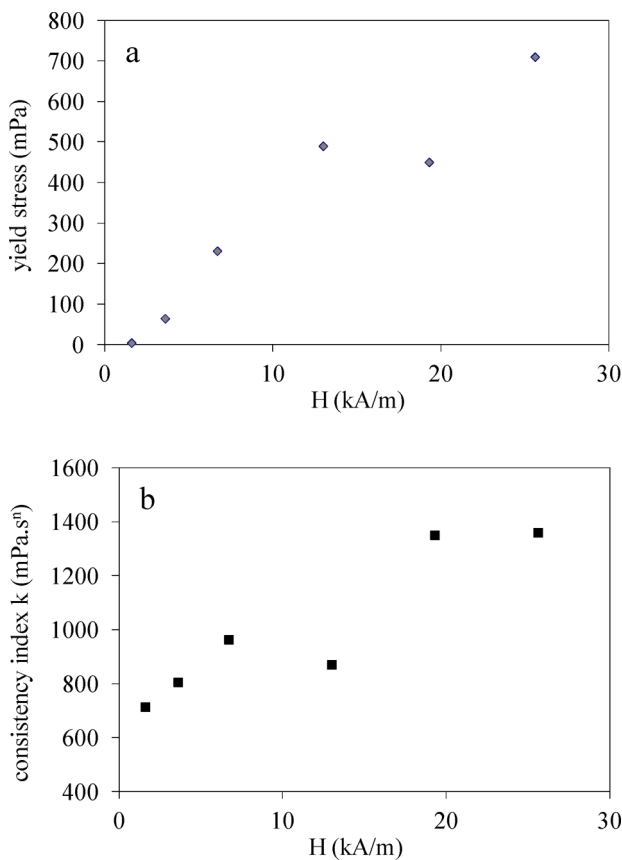


Figure 17. Variation of yield stress (a) and consistency index (b) as a function of magnetic field strength for aqueous solution of sodium alginate ($C_{\text{alg}} = 18 \text{ g L}^{-1}$) with magnetic NPs ($\Phi_{\text{NP-APTES}} = 1\%$).

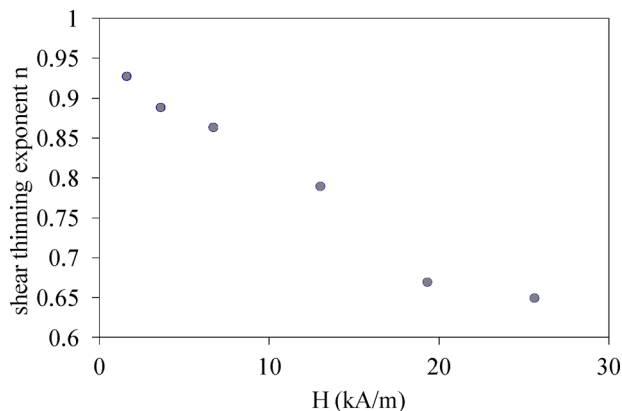


Figure 18. Variation of shear thinning exponent as a function of magnetic field strength for aqueous solution of sodium alginate ($C_{\text{alg}} = 18 \text{ g L}^{-1}$) with magnetic NPs ($\Phi_{\text{NP-APTES}} = 1\%$).

a structuration between the polymer and the particles appears, and this structure strengthens with the application and increase of the magnetic field. In order to analyze in detail these structures, optical microscopy observations have been carried out. Figure 19 shows the picture corresponding to an aqueous solution of sodium alginate ($C_{\text{alg}} = 18 \text{ g L}^{-1}$) with magnetic NPs ($\Phi_{\text{NP-APTES}} = 1\%$) for two values of magnetic field strength (3.2 and 23.9 kA m⁻¹).

At initial state t_0 (first column of Figure 19) without magnetic field ($H = 0 \text{ kA m}^{-1}$), clustered nanoparticles seem to be dispersed in the aqueous solution of sodium alginate. Under

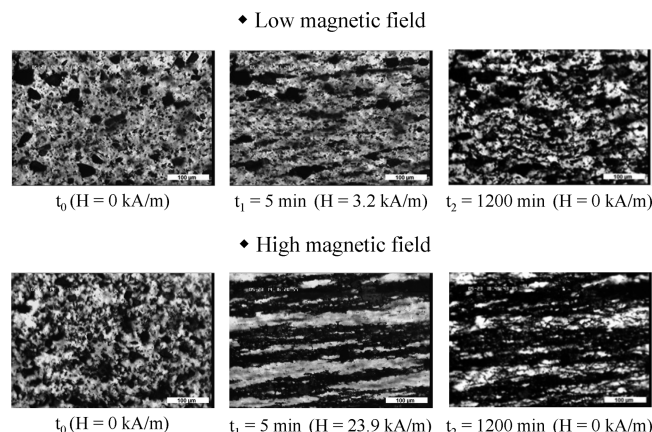


Figure 19. Optical microscopy under magnetic field application for aqueous solution of sodium alginate ($C_{\text{alg}} = 18 \text{ g L}^{-1}$) with magnetic NPs ($\Phi_{\text{NP-APTES}} = 1\%$). Bar scale 100 μm .

applied magnetic field (second column of Figure 19), black structures clearly appear and should correspond to sodium alginate chains with clustered nanoparticles aligned in the direction of the magnetic field. As expected, these structures are bigger for the highest value of magnetic field. Contrariwise to rheological measurements, the sodium alginate chains are not sheared during the observation time. Hence, when the magnetic field is switched off for 2 h (third column of Figure 19), clustered nanoparticles are not longer magnetized but structures different from the ones observed under applied magnetic field are still observed.

CONCLUSION

In this paper, novel magnetic sensitive nanocomposite biopolymer-based materials have been designed and studied. Magnetic nanoparticles of maghemite have been synthesized by the polyol process and further functionalized with 3-amino-propyltriethoxysilane bearing NH₂ functional groups and able to bind the nanoparticles through the ethoxy groups. Then, the produced nanohybrids have been introduced in aqueous sodium alginate solutions. A significant and reversible enhancement of viscoelastic moduli and viscosity at low shear rate has been clearly evidenced and could be explained by intramolecular electrostatic interactions between the positively charged NH₃⁺ groups present at the surface of the magnetic nanoparticles and the negatively charged carboxylate groups (COO⁻) of sodium alginate chains. This assumption is supported by microscopic observations showing magnetic-induced structures in the nanocomposite materials. The combination of magnetic properties of maghemite nanoparticles with the biocompatibility of sodium alginate suggests that these materials have a great potential to be used as drug delivery systems.

AUTHOR INFORMATION

Corresponding Author

*E-mail alain.ponton@univ-paris-diderot.fr (A.P.).

Notes

The authors declare no competing financial interest.

ACKNOWLEDGMENTS

This work was supported by the French Ministry of Research and National Center for Scientific Research. ANR (Agence

Nationale de la Recherche) and CGI (Commissariat à l'Investissement d'Avenir) are gratefully acknowledged for their financial support of this work through Labex SEAM (Science and Engineering for Advanced Materials and devices), ANR 11 LABX 086, ANR 11 IDEX 05 02.

(31) Volkova, O.; Bossis, G.; Guyot, M.; Bashtovoi, V.; Reks, A. J. *Rheol.* **2000**, *44*, 91–1004.

■ REFERENCES

- (1) Satarkar, N. S.; Biswal, D.; Hilt, J. Z. *Soft Matter* **2010**, *6*, 2364–2371.
- (2) Sarkar, S.; Guibal, E.; Quignard, F.; SenGupta, A. K. *J. Nanopart. Res.* **2012**, *14*:715, 1–24.
- (3) Govorov, A. O.; Richardson, H. H. *Nanotoday* **2007**, *2*, 30–38.
- (4) Wang, X.; Gu, H.; Yang, Z. *J. Magn. Magn. Mater.* **2005**, *293*, 334–340.
- (5) Viota, J. L.; Delgado, A. V.; Arias, J. L.; Duran, J. D. G. *J. Colloid Interface Sci.* **2008**, *324*, 199–204.
- (6) Kim, M. S.; Liu, Y. D.; Park, B. J.; You, C. Y.; Choi, H. J. *J. Ind. Eng. Chem.* **2012**, *18*, 664–667.
- (7) Wei, B.; Gong, X.; Jiang, W.; Qin, L.; Fan, Y. *J. Appl. Polym. Sci.* **2010**, *118*, 2765–2771.
- (8) Gannon, C. J.; Cherukuri, P.; Yakobson, B. I.; Cognet, J. L.; Kanzius, S.; Kittrell, C.; Weisman, R. B.; Pasquali, M.; Schmidt, H. K.; Smalley, R. E.; Curley, S. A. *Cancer* **2007**, *110*, 2654–2665.
- (9) Hsieh, D. S. T.; Langer, R.; Folkman, J. *Proc. Natl. Acad. Sci. U. S. A.* **1981**, *78*, 1863–1867.
- (10) Hu, S.-H.; Liu, T.-Y.; Liu, D.-M.; Chen, S.-Y. *Macromolecules* **2007**, *40*, 6786–6788.
- (11) Frimpong, R. A.; Fraser, S.; Hilt, J. Z. *J. Biomed. Mater. Res., Part A* **2007**, *80A*, 1–6.
- (12) Schild, H. G. *Prog. Polym. Sci.* **1992**, *17*, 163–249.
- (13) Satarkar, N. S.; Hilt, J. Z. *J. Controlled Release* **2008**, *130*, 246–251.
- (14) Xulu, P. M.; Filipcsei, G.; Zrinyi, M. *Macromolecules* **2000**, *33*, 1716–1719.
- (15) Hawkins, A. M.; Satarkar, N. S.; Hilt, J. Z. *Pharm. Res.* **2009**, *26*, 667–673.
- (16) Liu, T. Y.; Hu, S. H.; Liu, K. H.; Liu, D. M.; Chen, S.-Y. *J. Controlled Release* **2008**, *126*, 228–236.
- (17) Liu, T. Y.; Hu, S. H.; Liu, D. M.; Chen, S. Y. *Langmuir* **2006**, *22*, 5974–5978.
- (18) Basti, H.; Ben Tahar, L.; Smiri, L. S.; Herbst, F.; Vaulay, M. J.; Chau, F.; Ammar, S.; Benderbous, S. *J. Colloid Interface Sci.* **2010**, *341*, 248–254.
- (19) Hanini, A.; Schmitt, A.; Kacem, K.; Chau, F.; Ammar, S.; Gavard, J. *Int. J. Nanomed.* **2011**, *6*, 787–794.
- (20) Caruntu, D.; Cushing, B. L.; Caruntu, G.; O'Connor, C. *J. Chem. Mater.* **2005**, *17*, 3398–3402.
- (21) Lutterotti, L.; Matthies, S.; Wenk, H. R. *IUCr: Newslett. Comm. Powder Diffraction* **1999**, *21*, 14–15.
- (22) *The Iron Oxides. Structure, Properties, Reactions, Occurrence and Uses*; Cornell, R. M., Schwertmann, U., Eds.; John Wiley and Sons: New York, 1996.
- (23) Nakamoto, K. *Infrared and Raman Spectra of Inorganic and Coordination Compounds*, 4th ed.; Wiley Publisher: New York, 1986.
- (24) Dormann, J. L.; Fiorani, D.; Tronc, E. *Adv. Chem. Phys.* **1997**, *XC-VII*, 283–494.
- (25) Fiorani, D.; Testa, A. M.; Tronc, E.; Lucari, F.; D'Orazio, D.; Nogués, M. *J. Magn. Magn. Mater.* **2001**, *226*–230, 1942–1944.
- (26) Pereira, A. M.; Pereira, C.; Silva, A. S.; Schmool, D. S. *J. Appl. Phys.* **2011**, *109*, 114319.1–114319.5.
- (27) García-Otero, J.; Parto, M.; Rivas, J.; Bunde, A. *Phys. Rev. Lett.* **2000**, *84*, 167–170.
- (28) Rankin, P. J.; Ginder, J. M.; Klingenberg, D. J. *Curr. Opin. Colloid Interface Sci.* **1998**, *3*, 373–381.
- (29) Hong, R. Y.; Ren, Z. Q.; Han, Y. P.; Li, H. Z.; Zheng, Y.; Ding, J. *Chem. Eng. Sci.* **2007**, *62*, 5912–5924.
- (30) Ramos, J.; Klingenberg, D. J.; Hidalgo-Alvarez, R.; de Vicente, J. *J. Rheol.* **2011**, *55*, 127–152.